Journal of Energy Storage 107 (2025) 114983

Contents lists available at ScienceDirect

Journal of Energy Storage

journal homepage: www.elsevier.com/locate/est

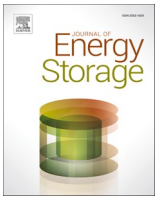

Research Papers

Porous silicon/carbon composites fabricated via microwave-assisted carbothermal shock for lithium-ion batteries

Chang-Hyun Cho [a,b,1], Won Ung Jeong [a,1], Jae Seok Jeong [a], Chang-Ha Lim [b], Jae-Kook Yoon [b], Chris Yeajoon Bon [b], Kap-Seung Yang [b,*], Min-Sik Park [a,*]

[a] Department of Advanced Materials Engineering for Information and Electronics, Integrated Education Institute for Frontier Science & Technology (BK21 Four), Kyung Hee University, 1732 Deogyeong-daero, Giheung-gu, Yongin-si 17104, Republic of Korea

[b] Rechargeable Battery Composite Materials R&D Center, Deca Material Inc., 224 Wanjusandan 6-rok, Bongdong-eup, Wanju-gun, Jeollabuk-do 55317, Republic of Korea

ARTICLE INFO

Keywords:
Silicon
Graphite
Porous structure
Lithium ion batteries
Carbothermal shock

ABSTRACT

To address the unstable characteristics of high-content Si anodes for lithium-ion batteries (LIBs), a novel approach is developed for creating a porous silicon@carbon (p-Si@C) composite using a fusible polyacrylonitrile copolymer (co-PAN). The p-Si@C composite is synthesized through a melt-extrusion process combined with microwave-assisted carbothermal shock. Prior to melt-extrusion, micro-sized Si (m-Si) and fusible co-PAN powders are blended in a blade mill. Following this, the mixture is subjected to carbothermal shock under microwave irradiation. Interestingly, the resulting composite features a porous structure where nano-sized Si (n-Si) particles are embedded within a porous carbon framework derived from the thermal decomposition of co-PAN. The n-Si content in the composite is estimated at 63.8 wt%, enabling a high reversible capacity (1891.6 mAh g^{-1}). For practical application, the p-Si@C composite (10 wt%) is physically blended with commercial graphite (90 wt%), delivering a reversible capacity of 535.1 mAh g^{-1}, approximately 1.5 times higher than commercial graphite. Moreover, it exhibits stable cycling performance, maintaining approximately 84.3 % of its capacity after 100 cycles. This porous architecture effectively accommodates the volume variation of n-Si particles and suppresses the unstable solid electrolyte interphase (SEI) formation, leading to enhanced structural durability during cycling.

1. Introduction

As the leading energy storage technology, lithium-ion batteries (LIBs) are the commercial choice for electric vehicles (EVs) owing to their superior energy density and operational efficiency. To further improve EV driving performance, there is a strong demand for advanced materials that can increase the practical energy density of LIBs [1,2]. The development of high-capacity anodes is therefore crucial to replace commercial graphite with a low theoretical capacity (~372 mAh g^{-1}) [3,4]. In this regard, silicon (Si) is a potential candidate, thanks to its exceptionally high capacity (~3580 mAh g^{-1}, $Li_{15}Si_4$), about 10 times greater than graphite [5–7]. Si reacts with Li^+ through electrochemical alloying/de-alloying, enabling the formation/decomposition of Li_xSi alloys at ~0.4 V vs. Li/Li^+ [8–10]. Despite these advantages, Si anodes experience over 300 % volume expansion when fully charged [11–13]. This significant expansion induces mechanical stress, leading to Si particle pulverization and abnormal growth of the solid electrolyte interphase (SEI), resulting in the continuous loss of reversible capacity during cycling [14–16]. To address this challenge, various structural engineering strategies have been proposed to suppress volume expansion and ensure cycling stability of Si-based anodes.

Chan et al. demonstrated that reducing the particle size of Si effectively mitigates undesirable particle pulverization during cycling by relieving mechanical strain [17]. In practice, Si particles smaller than 150 nm exhibited stable cycling performance without pulverization [18,19]. Unfortunately, the increased surface area of nano-sized Si (n-Si) particles promoted unstable SEI formation and irreversible Li^+ consumption during cycling [20–22]. Alternatively, structural engineering with conductive carbonaceous materials has been shown to enhance the cycling stability of Si-based anodes. Various Si@C composites hold great

* Corresponding authors.
E-mail addresses: ksyang@decamaterial.com (K.-S. Yang), mspark@khu.ac.kr (M.-S. Park).
[1] These authors contributed equally to this work.

https://doi.org/10.1016/j.est.2024.114983
Received 13 October 2024; Received in revised form 27 November 2024; Accepted 6 December 2024
Available online 13 December 2024

potential for enhancing the practical energy density of LIBs by increasing reversible capacity and ensuring cycling stability. This improvement is due to the functionalities of carbonaceous materials to accommodate the volume variations of Si and maintain conductive pathways for Li^+ and electrons [23–25]. Nevertheless, the dimensional changes in Si@C composites at the electrode level do not yet meet rigorous industrial requirements.

As part of ongoing efforts to develop highly reliable Si@C composites, PAN-derived porous carbon structure attracted significant attention to ensure the dimensional stability of Si@C composites. During the carbonization process of PAN, its low carbon yield leads to the formation of a porous structure, which accommodates volume change effectively with improved cycle stability [26,27]. The free spaces or voids act as buffers, accommodating the large volume variations of Si and relieving mechanical strain, thereby minimizing dimensional changes at the electrode level during cycling [27,28]. Moreover, the cyclization of nitrile groups in PAN facilitates the development of π-π conjugation, which provides sufficient pathways for electrolyte penetration, and ensures uniform Li^+ transport throughout the electrode [29–32]. However, current synthesis processes for porous Si@C composites are often complex and time-consuming, making it critical to develop more cost-effective processes suitable for mass production.

Herein, we propose an innovative and cost-effective synthesis method for a porous Si@C composite for realizing high-energy LIBs. A robust p-Si@C composite can be fabricated through a melt-extrusion process of micro-sized Si (m-Si) and fusible polyacrylonitrile copolymer (co-PAN) powders, followed by a microwave-assisted carbothermal shock. During the carbothermal shock process, m-Si particles are pulverized into n-Si particles, while the fusible co-PAN, with its low carbonization yield, forms a porous carbon framework encapsulating the n-Si particles. This unique structural configuration is expected to enhance both reversible capacity and dimensional stability of the p-Si@C composite, while providing excellent cycling performance. We believe that this approach offers greater design flexibility for high-capacity anodes, addressing key challenges in the development of advanced LIBs.

2. Experimental details

2.1. Materials preparation

The polyacrylonitrile copolymer (co-PAN, synthesized at Deca Material Co., Korea, M_w = 220,000) was homogeneously blended with micro-sized Si (m-Si) particles. A mixture comprising 46 wt% m-Si and 54 wt% fusible co-PAN was extruded using a single-screw extruder at temperatures exceeding the melting point of 180 °C. Following extrusion, the resulting composite was stabilized at 280 °C with air blowing, followed by a carbonization process. To prepare the p-Si@C composite, a carbothermal shock process was employed, utilizing microwave irradiation (2.4–2.5 GHz) at a power of 3.1 kW [33–37]. For comparative purposes, an n-Si@C composite was also synthesized with n-Si particles and coal-tar pitch by carbonization at 1000 °C for 2 h in an Ar flow. The content of n-Si particles was meticulously controlled, taking into account the carbonization yield of the coal-tar pitch.

2.2. Structural characterization

For morphological investigations, a field-emission scanning electron microscope (FESEM, Carl Zeiss) was utilized. Microstructural characterizations were conducted using a transmission electron microscope (TEM, ARM—200F). Structural characteristics were analyzed through Raman spectroscopy (Olympus, BX 43) and X-ray diffraction (XRD, Empyrean). Surface chemistry and chemical bonding were examined via X-ray photoelectron spectroscopy (XPS, Thermo Scientific K-alpha). Compositional analysis was performed using thermogravimetric analysis (TGA, PerkinElmer). The particle size distribution was assessed with a particle size analyzer (PSA, NPA252). Additionally, surface area and pore volume were measured using a surface area and porosity analyzer (Micromeritics, Tristar 3020) based on the Brunauer-Emmett-Teller (BET) method.

2.3. Electrochemical measurement

The active materials (90 wt%) were homogeneously mixed with a conductive agent (Super-P, 5 wt%) and a polyvinylidene fluoride (PVDF, 5 wt%) binder in an *N*-methyl-2-pyrrolidone (NMP) solvent. The resulting slurry was cast onto copper foil (10 μm). The anodes were designed with a loading level of 4.0 mg cm^{-2} and an electrode density of 1.5 g cm^{-3}. Using a polyethylene (PE) membrane and Li metal foil, half-cells were assembled. The electrolyte, 1 M $LiPF_6$ dissolved in a solvent mixture composed of ethylene carbonate (EC), ethyl methyl carbonate (EMC), and dimethyl carbonate (DMC) (3:5:2 *v*/v), was added with 5 wt % fluoroethylene carbonate (FEC). Electrochemical performance was evaluated between 0.01 and 1.5 V vs. Li/Li^+ at various current densities (0.2–3.0C). For full-cell assembly, cathodes were fabricated by casting a slurry of $LiNi_{0.8}Co_{0.1}Mn_{0.1}O_2$ (NCM, 96 wt%), Super-P (2 wt%), and PVDF (2 wt%) onto aluminum foil (15 μm). Full-cells were designed to achieve an areal capacity of 2.2 mAh cm^{-2} (N/P ratio = 1.1), and cycled between 2.5 and 4.2 V at 0.5C.

3. Results and discussion

The m-Si and fusible co-PAN powders were utilized as starting materials to develop a porous p-Si@C composite. The unique physicochemical properties of co-PAN facilitate the spontaneous formation of a porous carbon matrix during carbonization, induced by microwave-assisted carbothermal shock (Fig. S1). Differential scanning calorimetry (DSC) and TGA curves of homopolymer polyacrylonitrile (homo-PAN) and fusible co-PAN (Fig. S2) indicate that co-PAN exhibits melting behavior between 80 and 159 °C, with a cyclization reaction temperature of 80 °C, while homo-PAN shows no melting behavior. This suggests that co-PAN is fusible and possesses lower thermal stability compared to homo-PAN. These distinct thermal properties imply that fusible co-PAN experiences significant mass loss during carbonization, resulting in a porous carbon framework above the cyclization temperature.

We further investigated the structural evolution of fusible co-PAN during the microwave-assisted carbothermal shock (Fig. S3). After this process, the crystalline (100) peak of the *co*-PAN polymer shifted to a higher Bragg angle at 2θ = 43.7°, indicating the formation of more ordered carbon structures [38]. The increased intensities of the crystalline (002) and (100) peaks at 2θ = 25.5° and 43.7°, respectively, further confirm that microwave-assisted carbothermal shock promotes the crystallization of the carbon phase derived from co-PAN [39]. This process effectively transforms co-PAN into a well-ordered carbon structure, contributing to the spontaneous formation of the porous carbon matrix.

Fig. 1a describes a schematic of the p-Si@C composite obtained by a microwave-assisted carbothermal shock method using m-Si and co-PAN powders. A blend of m-Si and co-PAN powders was extruded through a single-screw extruder, followed by microwave-induced carbothermal shock. Fig. 1b displays the spherical morphology of the resulting p-Si@C composite (~20 μm), with n-Si particles (~100 nm) successfully embedded and uniformly dispersed in an amorphous carbon matrix (Fig. 1c). During the carbothermal shock, the m-Si particles (~5 μm) fractured into n-Si particles (~ 50 nm), which were uniformly encapsulated by the porous carbon matrix derived from co-PAN (Fig. S4). Cross-sectional SEM images confirm the formation of abundant internal pores (~7.7 nm in size) within the p-Si@C composite, resulting from the thermal decomposition of co-PAN under microwave-assisted carbothermal shock (Fig. 1d). For comparison, a non-porous n-Si@C composite having a similar morphology and Si content was also prepared (Fig. S5).

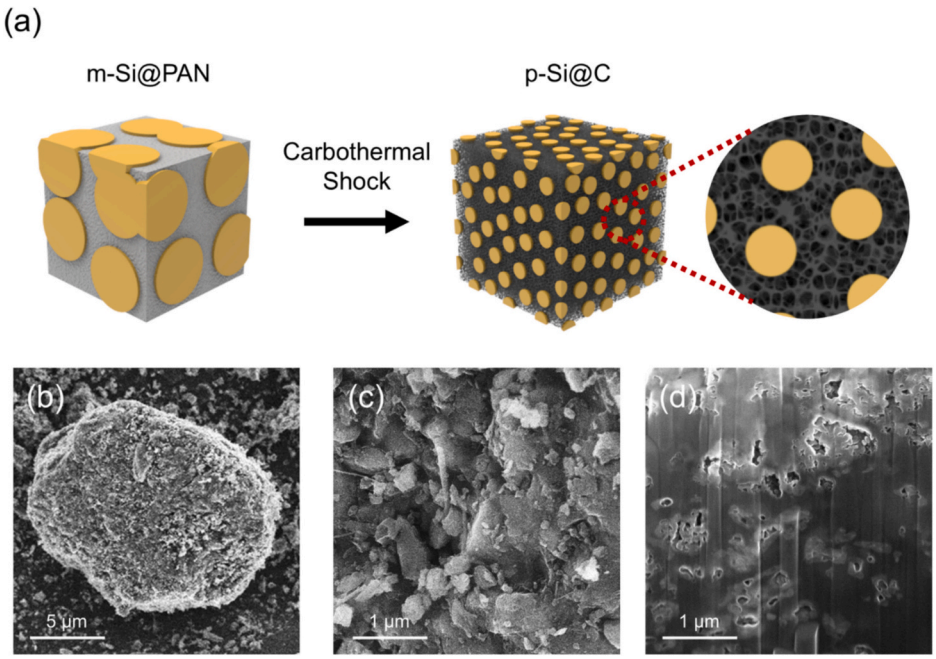

Fig. 1. (a) Synthesis process of the p-Si@C composite via carbothermal shock through microwave induction. (b-c) FESEM images of the p-Si@C composite at different magnifications. (d) Cross-sectional FESEM image of the p-Si@C composite.

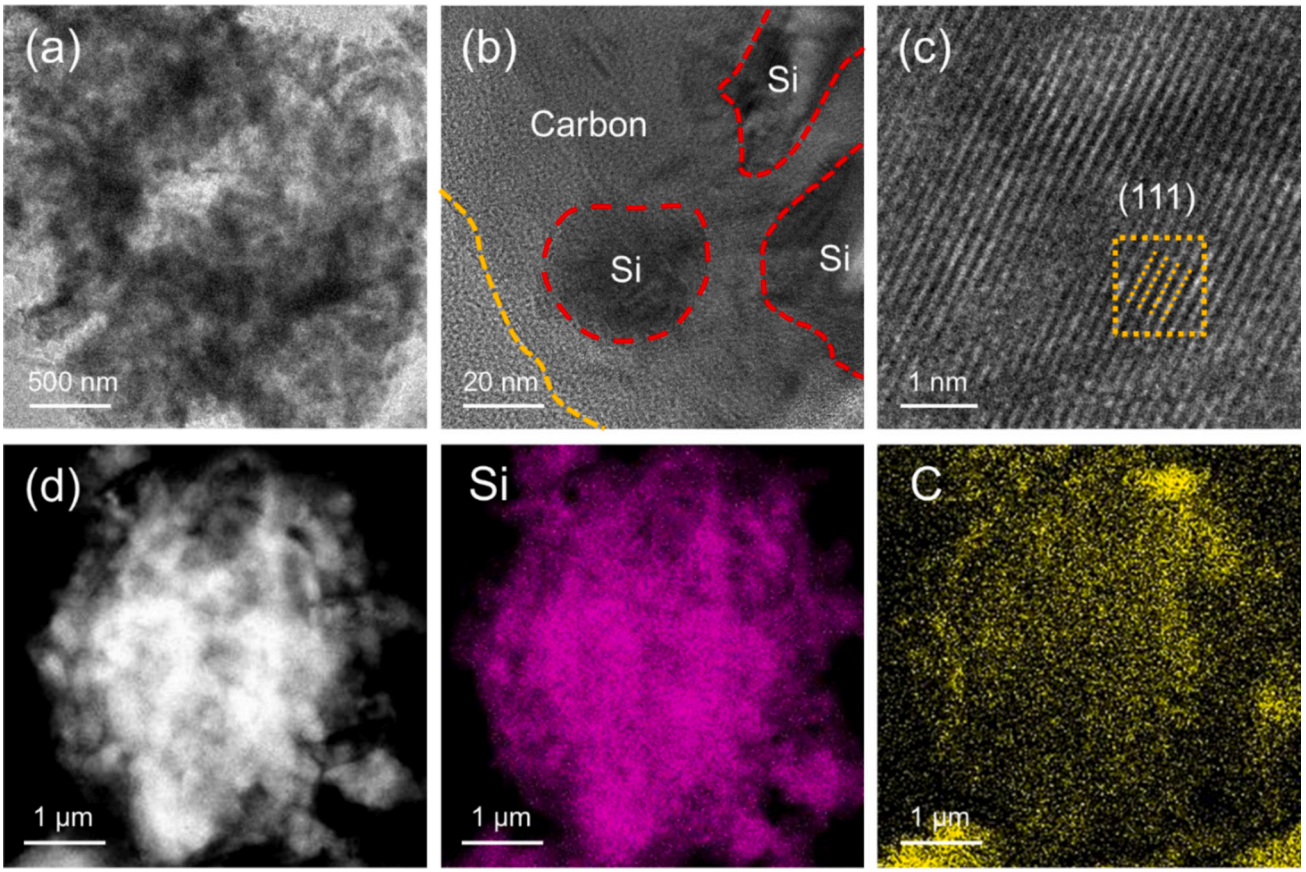

Fig. 2. (a) Bright-field TEM image of the p-Si@C composite. (b) HRTEM image of the p-Si@C composite. (c) *d*-spacing measurements of n-Si particles within the p-Si@C composite. (d) Dark-field TEM image of the p-Si@C composite with EDS elemental mappings for silicon (magenta) and carbon (yellow). (For interpretation of the references to colour in this figure legend, the reader is referred to the web version of this article.)

TEM observations in Figs. 2a-b further confirm the successful embedding of n-Si particles into the porous carbon matrix derived from co-PAN. High-resolution TEM reveals crystalline n-Si particles (~50 nm) encapsulated by an amorphous carbon phase (Fig. 2b). Note that the n-Si particles exhibit a lattice structure with a d-spacing of 0.31 nm, corresponding to the interplanar distance of the (111) plane in crystalline Si (Fig. 2c) [40]. Elemental mappings from EDS (Fig. 2d) support the compositional arrangement of Si (magenta) and C (yellow) within the p-Si@C composite.

Fig. 3a compares the powder XRD patterns of both p-Si@C and n-Si@C composites prepared by different synthesis processes. In the case of n-Si@C composite, typical reflections of crystalline Si (JCPDS 27–1402) were evident [41]. In contrast, the p-Si@C composite has additional peaks at $2\theta = 35.7°$, 41.5°, 60.1°, and 72.0°, corresponding to the crystalline β-SiC phase (JCPDS 75-0254) [42]. The Raman spectra (Fig. 3b) indicate that the p-Si@C composite has a higher I_D/I_G intensity ratio of 1.25 compared to the n-Si@C composite (1.06), calculated from the D-band (1350 cm^{-1}) and G-band (1590 cm^{-1}), suggesting a higher degree of crystallinity in the porous carbon matrix resulting from the microwave-assisted carbothermal shock [43]. Additionally, the formation of crystalline β-SiC is further examined by comparing the XPS Si 2p spectra after deconvolution based on C 1s (284.5 eV). Unlike the n-Si@C composite, a noticeable signal for Si—C chemical bond is observed at 100.7 eV after the microwave-assisted carbothermal shock (Fig. 3c) [44]. The growth of the β-SiC phase is primarily attributed to the high thermal energy generated during the carbothermal shock, which promotes the chemical reaction of n-Si particles with amorphous carbon in the p-Si@C composite. From a structural perspective, the presence of the β-SiC phase is expected to enhance the adhesion of n-Si particles to the porous carbon matrix, effectively accommodating the volume variation of n-Si particles and thereby improving the dimensional stability upon repeated cycling. On the other hand, the electrical conductivities of both

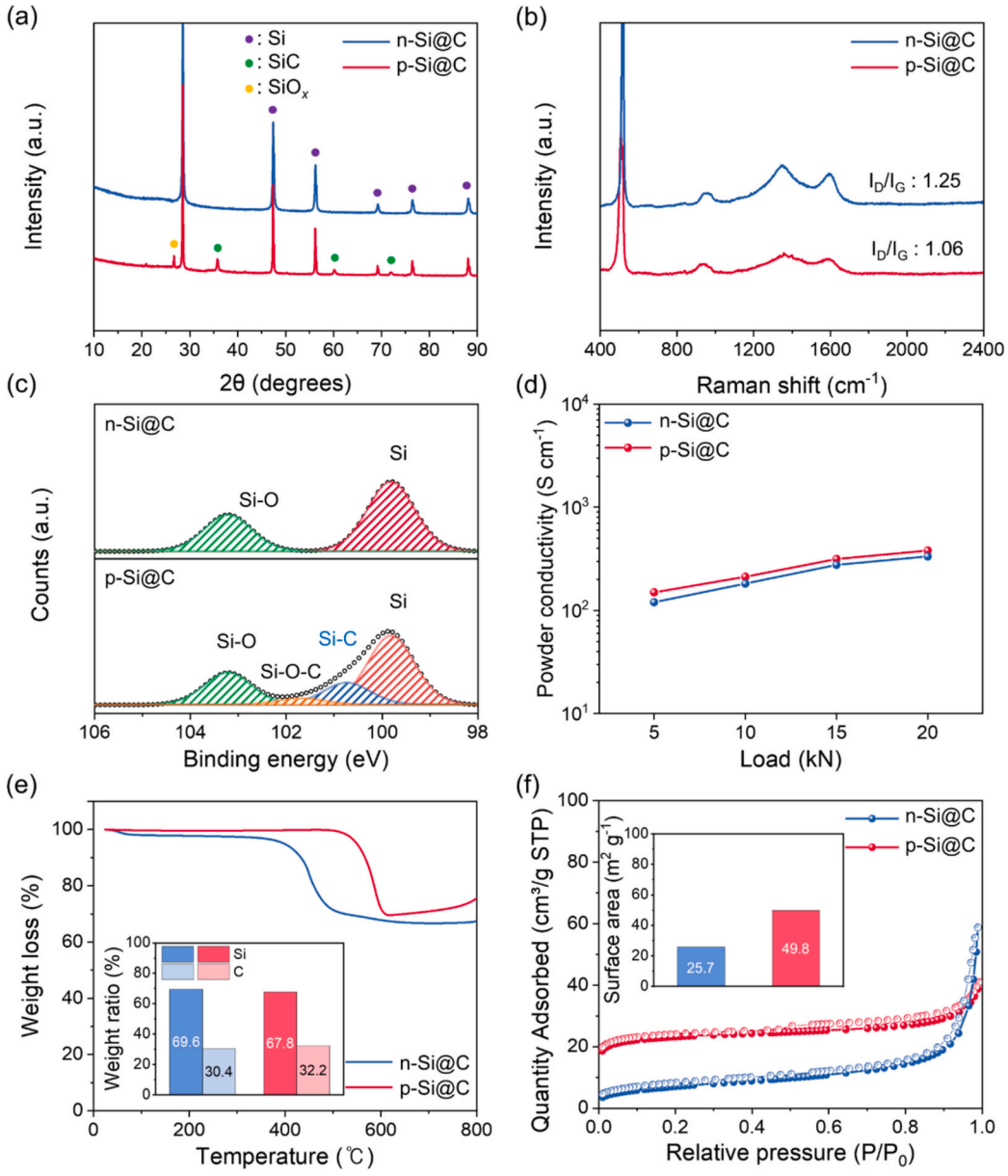

Fig. 3. (a) Powder XRD patterns of n-Si@C and p-Si@C composites. (b) Raman spectra of n-Si@C and p-Si@C composites. (c) XPS profiles of Si 2p spectra for n-Si@C and p-Si@C composites. (d) Electrical conductivities of n-Si@C and p-Si@C composites at various applied pressures. (e) TGA curves of n-Si@C and p-Si@C composites measured under a flow of O_2 gas, with corresponding derivative thermogravimetry (DTG) profiles in the inset. (f) N_2 adsorption–desorption isotherms of n-Si@C and p-Si@C composites, with surface area in the inset.

composites were measured using a power-resistivity measurement system. Notably, the p-Si@C composite exhibited higher electrical conductivity (380.7 S cm^{-1}) compared to the n-Si@C composite (333.9 S cm^{-1}) under an applied pressure of 20 kN (Fig. 3d).

The n-Si fractions of the n-Si@C and p-Si@C composites were verified through TGA/DTG analyses (Fig. 3e). In principle, the weight loss (350–600 °C) corresponds to the oxidation of C to CO_2, while the weight gain (700–800 °C) indicates the oxidation of Si to SiO_x [45]. The carbon oxidation temperature in the p-Si@C composite is relatively higher than that in the n-Si@C composite (Fig. S6). From the DTG and TGA profiles, we estimated the content of n-Si to be 67.8 wt% in the p-Si@C composite and 69.6 wt% for the n-Si@C composite. The higher oxidation temperature and electrical conductivity of the p-Si@C composite are attributed to the increased crystallinity of the porous carbon matrix.

According to the N_2 isotherms (Fig. 3f), the p-Si@C composite has a surface area of 49.8 m^2 g^{-1} and a total pore volume of 0.08 cm^3 g^{-1}, both of which are greater than those of the n-Si@C composite (25.7 m^2 g^{-1} and 0.04 cm^3 g^{-1}). From the Barrett-Joyner-Halenda (BJH) curves (Fig. S7), we observed that the p-Si@C composite contains a higher fraction of internal micropores (<2 nm) compared to the n-Si@C composite. This indicates that the p-Si@C composite developed abundant internal pores during the carbonization process, facilitated by the microwave-assisted carbothermal shock, thereby contributing to its increased surface area and porosity.

The electrochemical performance of the p-Si@C anode was evaluated over a voltage range of 0.01–1.5 V vs. Li/Li^+. As compared in Fig. S8a, the p-Si@C anode exhibited electrochemical behavior similar to that of the n-Si@C anode. It offered a high reversible capacity of 1891.6 mAh g^{-1} and the initial coulombic efficiency was estimated to be 75.6 % during the first cycle. For practical application, we prepared a blended anode composed of the p-Si@C composite (10 wt%) and graphite (90 wt%), denoted as p-Si@C-G. The blended p-Si@C-G anode

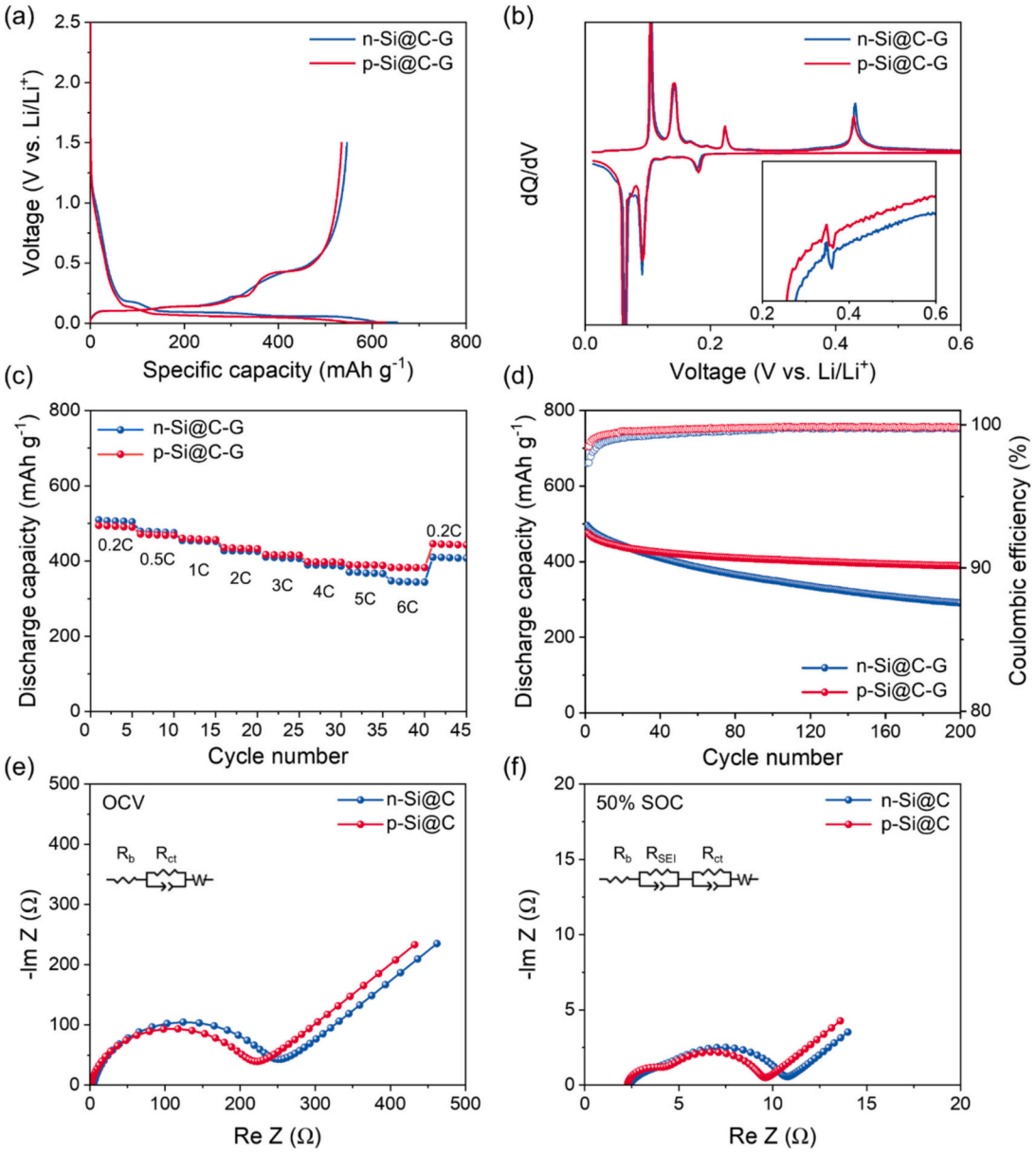

Fig. 4. Electrochemical performances of half-cells assembled with n-Si@C-G and p-Si@C-G anodes: (a) Galvanostatic voltage profiles recorded at a charging current density of 0.05C (1C = 535 mA g^{-1}) and (b) corresponding differential voltage (dQ/dV) profiles during the first cycle. (c) Comparison of rate capabilities at various charging C-rates of 0.2, 0.5, 1, 2, 3, 4, 5, and 6C. (d) Cyclic performance at 0.5C charging and 0.5C discharging for 200 cycles. Nyquist plots with equivalent circuit models (insets) for n-Si@C and p-Si@C anodes at (e) open circuit voltage (OCV) and (f) 50 % state of charge (SOC).

demonstrated a reversible capacity of 535.1 mAh g^{-1}, approximately 1.5 times higher than graphite anode (Fig. 4a). Fig. 4b displays the corresponding differential voltage profiles, revealing two distinct plateaus: one at around 0.4 V vs. Li/Li^+, representing the alloying/de-alloying reactions of n-Si, and another at about 0.2 V vs. Li/Li^+ for the intercalation/de-intercalation reactions of graphite. The second plateau was extended by increasing the fraction of p-Si@C composite, due to the additional contribution of n-Si (Fig. S8b).

As expected, the p-Si@C-G anode demonstrated superior rate capability (Fig. 4c), showing improved capacity retention across current densities ranging from 0.2 to 6C. In practice, the p-Si@C-G anode retained 77.4 % of its reversible capacity at 6C relative to 0.2C, whereas the n-Si@C-G anode showed only 68.2 % under the same conditions. This can be mainly attributed to the porous structural features of the p-Si@C composite, which effectively accommodate the volume changes of n-Si particles while maintaining stable conduction pathways for Li^+ and electrons during cycling. Furthermore, the capacity retention of the blended p-Si@C-G anode was estimated to be 84.3 % after 100 cycles and continued to exhibit stable cycling performance over 200 cycles at 0.5C (Fig. 4d). However, the n-Si@C-G anode experienced significant capacity loss due to irreversible Li^+ consumption from particle pulverization and continuous SEI formation during the initial 30 cycles. Compared with previous studies (Table S1), the p-Si@G-C anode demonstrated superior electrochemical performance, highlighting remarkable advancements.

Nyquist plots of the p-Si@C and n-Si@C anodes were recorded at different states of charge (SOCs). At open circuit voltage (OCV), both anodes exhibited a semi-circle in the low-frequency region (Fig. 4e). Compared to the n-Si@C anode, the p-Si@C anode demonstrated relatively smaller contact resistance (R_b) and charge transfer resistance (R_{ct}). This is because the p-Si@C anode has a larger electrochemical active surface area arising from its porous architecture. At 50 % SOC (Fig. 4f), an additional semi-circle appeared in the low-frequency region, indicating film resistance (R_f) associated with SEI formation, alongside a decrease in R_{ct} values [46,47]. Remarkably, the p-Si@C anode showed a smaller R_{ct} value (7.8 Ω) compared to the n-Si@C anode (8.8 Ω).

We performed a post-mortem analysis to examine the structural changes of the p-Si@C composite. After cycling, the surface of the n-Si@C-G anode was roughened due to the particle pulverization of n-Si particles after 100 cycles (Fig. 5a). This structural degradation reduces particle contact and leads to a loss of conductivity, resulting in continuous capacity fading during cycling. In contrast, the p-Si@C-G anode still maintained a relatively clean surface even after 100 cycles (Fig. 5b).

XPS analysis was also conducted to further investigate the chemical composition and fraction of the SEI layers onto the anodes after cycling. The C 1s spectra revealed the presence of Li_2CO_3 and $ROCO_2Li$ as common SEI components. Comparing the p-Si@C-G (Fig. 5c) and n-Si@C-G (Fig. 5d) anodes, we found that the p-Si@C-G anode possesses a relatively lower fraction of SEI layer, as the porous carbon matrix encapsulates the n-Si particles, preventing their direct exposure to the electrolyte. These observations are supported by the Nyquist plots of both blended anodes, which reflect the influence of the SEI layer (Fig. S9). Before cycling, the p-Si@C-G anode had a lower R_b value than the n-Si@C-G anode due to its higher specific surface area. Interestingly, the p-Si@C-G anode showed a lower R_f value compared to the n-Si@C-G anode after 100 cycles, indicating less formation of SEI components, which is consistent with the suppression of continuous SEI layer growth in the p-Si@C-G anode.

For comparative purposes, full-cells assembled with an NCM cathode were cycled in a voltage range of 2.5–4.2 V at 0.5C (1C = 195 mA g^{-1}). Fig. 6a compares the voltage profiles of both n-Si@C-G and p-Si@C-G full-cells, showing similar electrochemical behaviors. As illustrated in Fig. 6b, the reversible capacity of the p-Si@C-G full-cell was comparable to the n-Si@C-G full-cell. Although the initial coulombic efficiency of the p-Si@C-G full-cell was slightly reduced due to the porous architecture of the p-Si@C composite, it did not significantly compromise the practical energy density. In practice, the p-Si@C-G full-cell exhibited improved coulombic efficiencies and maintained stable cycling performance (Fig. 6c). While the n-Si@C-G full-cell showed noticeable capacity reduction, the p-Si@C-G full-cell achieved about 80.3 % capacity

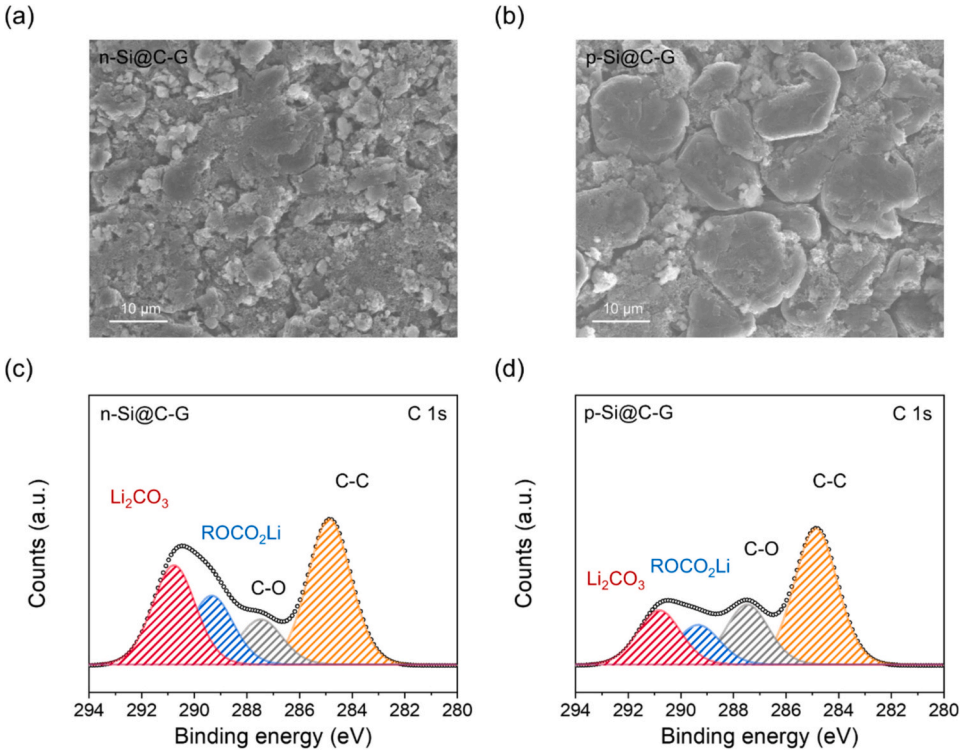

Fig. 5. Top view FESEM images of (a) n-Si@C-G and (b) p-Si@C-G anodes after 100 cycles. XPS C 1s profiles of (c) n-Si@C-G and (d) p-Si@C-G anodes after 100 cycles.

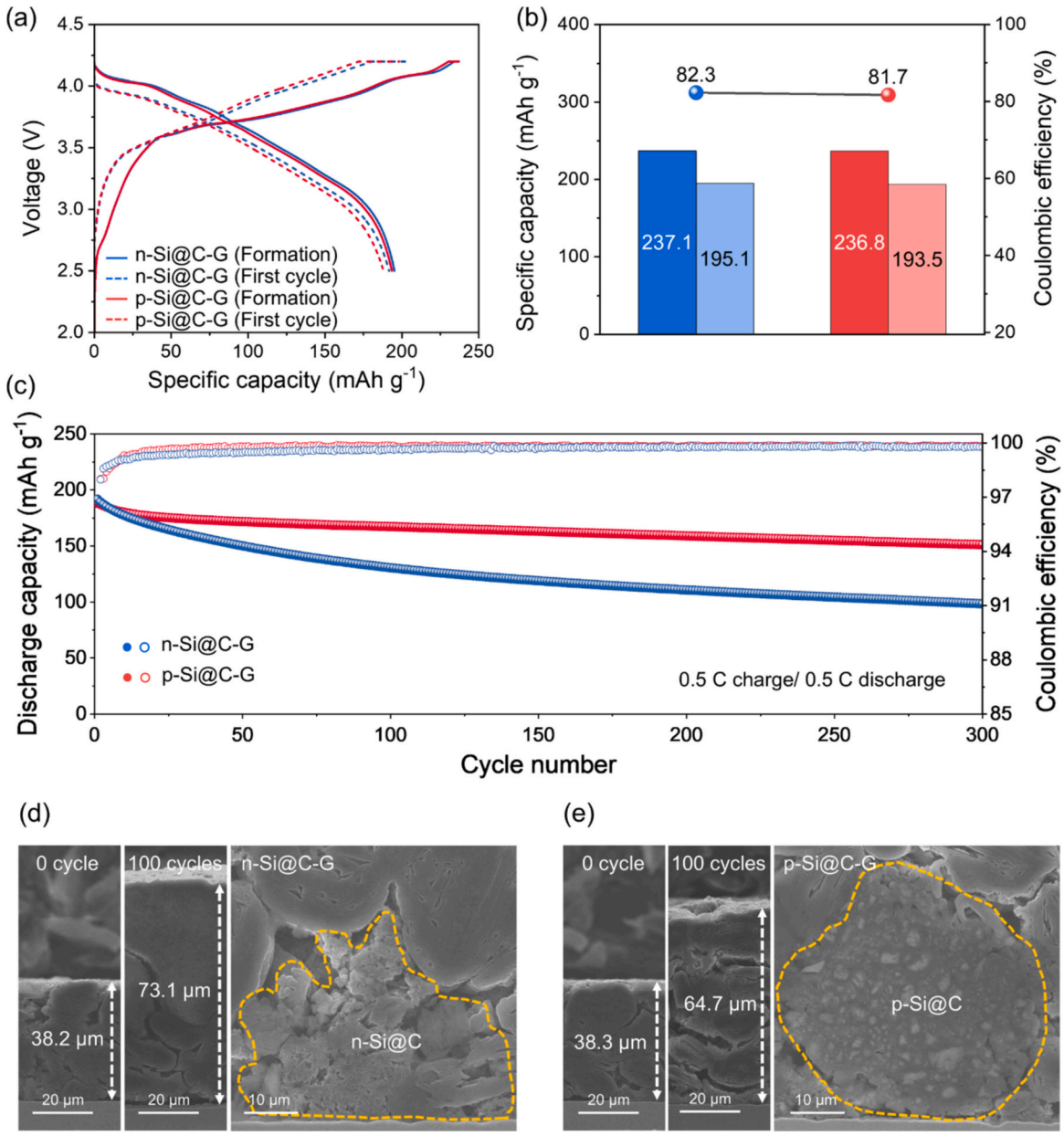

Fig. 6. Electrochemical performances of full-cells assembled with n-Si@C-G and p-Si@C-G anodes, each with an areal capacity of 2.2 mAh cm^{-2}: (a) Galvanostatic voltage profiles in the voltage range of 2.5–4.2 V at selected cycles. (b) Comparisons of specific capacity and coulombic efficiency during the first cycle. (c) Cycle performance at 0.5C charging and discharging over 300 cycles. Cross-sectional FESEM images of (d) n-Si@C-G and (e) p-Si@C-G anodes after 100 cycles in full-cells.

retention even after 300 cycles, without significant capacity loss. This improvement is attributed to the porous carbon matrix, which effectively encloses the n-Si particles, suppressing particle pulverization and continuous SEI formation during cycling. These results support that the p-Si@C composite can be practically utilized to enhance the reversible capacity as well as cycling stability of high-energy LIBs.

The dimensional stability of the p-Si@C-G anode was also investigated by comparing the electrode thickness after cycling. The thickness of the n-Si@C-G anode increased to 73.1 μm, indicating a 91 % expansion (Fig. 6d), while the p-Si@C-G anode maintained a thickness of 64.7 μm even after cycling (Fig. 6e). Furthermore, the n-Si particles remained encapsulated by the porous carbon matrix in the p-Si@C composite without pulverization. However, the n-Si particles were observed to extrude from the carbon layer and become exposed in the n-Si@C composite. As expected, the porous architecture of the p-Si@C composite enhances dimensional stability by accommodating volume changes and effectively relaxing the strain of the n-Si particles, resulting in superior cycling performance with minimal loss of reversible capacity during cycling.

4. Conclusions

In this study, we proposed a facile synthesis of a porous p-Si@C composite through carbothermal shock using microwave irradiation for practical use in high-energy LIBs. This innovative and cost-effective synthesis strategy is more suitable for mass production than conventional approaches. To develop the porous p-Si@C composite, m-Si and fusible co-PAN was mixed and extruded using a single-screw extruder, ensuring homogeneous mixing and enhancing contact between the m-Si and co-PAN above the melting temperature of 180 °C. During the microwave-assisted carbothermal shock, fusible co-PAN melted and decomposed, subsequently crystallizing while facilitating the

pulverization of m-Si into n-Si particles. The resulting p-Si@C composite contains n-Si particles (63.8 wt%) encapsulated by a porous carbon matrix (36.2 wt%) derived from co-PAN. In practice, the p-Si@C anode demonstrated a high reversible capacity of 1891.6 mAh g^{-1}. The feasibility of the p-Si@C composite was further examined by blending it with graphite (1:9 by weight), resulting in a blended p-Si@C-G anode that showed excellent cycling stability. Moreover, the p-Si@C-G full-cell achieved about 80.3 % capacity retention even after 300 cycles. It demonstrated remarkable dimensional stability, with minimal particle pulverization and electrode expansion after cycling. Our approach provides a practical guideline for developing high-content silicon anodes for advanced LIBs.

CRediT authorship contribution statement

Chang-Hyun Cho: Methodology, Investigation, Conceptualization. **Won Ung Jeong:** Formal analysis, Data curation, Conceptualization. **Jae Seok Jeong:** Methodology, Investigation. **Chang-Ha Lim:** Methodology, Conceptualization. **Jae-Kook Yoon:** Investigation, Data curation. **Chris Yeajoon Bon:** Investigation, Conceptualization. **Kap-Seung Yang:** Writing – original draft, Supervision, Conceptualization. **Min-Sik Park:** Writing – original draft, Supervision, Conceptualization.

Declaration of competing interest

The authors declare that they have no known competing financial interests or personal relationships that could have appeared to influence the work reported in this paper.

Acknowledgements

This work was supported by the National Research Foundation of Korea [NRF-2021M3H4A1A02048137 and NRF-2018R1A5A1025594] of the Ministry of Science and ICT, Republic of Korea.

Appendix A. Supplementary data

Supplementary data to this article can be found online at https://doi.org/10.1016/j.est.2024.114983.

Data availability

Data will be made available on request.

References

[1] A. Tomazewska, Z. Chu, X. Feng, S. Okane, X. Liu, J. Chen, C. Ji, E. Ender, R. Li, L. Liu, Y. Li, S. Zheng, S. Vetterlein, M. Gao, J. Du, M. Parkes, M. Ouyang, M. Marinescu, B. Wu, Lithium-ion battery fast charging: a review, eTransportation 1 (2019) 100011, https://doi.org/10.1016/j.etran.2019.100011.

[2] H. Wu, G. Chan, J.W. Choi, I. Ryu, Y. Yao, M.T. McDowell, S.W. Lee, A. Jackson, Y. Yang, L. Hu, Y. Cui, Stable cycling of double-walled silicon nanotube battery anodes through solid–electrolyte interphase control, Nat. Nanotechnol. 7 (2012) 310–315, https://doi.org/10.1038/nnano.2012.35.

[3] H. Zhang, Y. Yang, D. Ren, L. Wang, X. He, Graphite as anode materials: fundamental mechanism, recent progress and advances, Energy Storage Mater. 36 (2021) 147–170, https://doi.org/10.1016/j.ensm.2020.12.027.

[4] W. Luo, X. Chen, Y. Xia, M. Chen, L. Wang, Q. Wang, W. Li, J. Yang, Surface and Interface engineering of silicon-based anode materials for Lithium-ion batteries, Adv. Energy Mater. 7 (2017) 1701083, https://doi.org/10.1002/aenm.201701083.

[5] M. Wetjen, S. Solchenbach, D. Pritzl, J. Hou, V. Tileli, H.A. Gasteiger, Morphological changes of silicon nanoparticles and the influence of cutoff potentials in silicon-graphite *electrodes*, J. Electrochem. Soc. 165 (2018) A1503–A1514, https://doi.org/10.1149/2.1261807jes.

[6] C. Gan, X. Ye, S. Zhang, J. Chen, W. Wen, Y. Liu, D.L. Peng, L. Tang, X. Luo, Current density induced growth of $Li_{15}Si_4$ alloy in silicon-carbon anodes during first lithiation process, J. Energy Storage 41 (2021) 102930, https://doi.org/10.1016/j.est.2021.102930.

[7] F. Luo, B. Liu, J. Zheng, G. Chu, K. Zhong, H. Li, X. Huang, L. Chen, Nano-silicon/carbon composite anode materials towards practical application for next generation Li-ion batteries, J. Electrochem. Soc. 162 (14) (2015) A2509–A2528, https://doi.org/10.1149/2.0131514jes.

[8] L.F. Cui, Y. Yang, C.M. Hsu, Y. Cui, Carbon−silicon core−shell nanowires as high capacity electrode for lithium ion batteries, Nano Lett. 9 (2009) 3370–3374, https://doi.org/10.1021/nl901670t.

[9] C. Gan, C. Zhang, W. Wen, Y. Liu, J. Chen, Q. Xie, X. Luo, Enhancing delithiation reversibility of $Li_{15}Si_4$ alloy of silicon nanoparticle-carbon/graphite anode materials for stable-cycling lithium ion batteries by restricting the silicon particle size, ACS Appl. Mater. Interfaces 11 (2019) 35809–35819, https://doi.org/10.1021/acsami.9b13750.

[10] M. Ashuri, Q. He, L.L. Shaw, Silicon as a potential anode material for Li-ion batteries: where size, geometry and structure matter, Nanoscale 8 (2016) 74, https://doi.org/10.1039/c5nr05116a.

[11] M.T. McDowell, I. Ryu, S.W. Lee, C. Wang, W.D. Nix, Y. Cui, Studying the kinetics of crystalline silicon nanoparticle Lithiation with in situ transmission electron microscopy, Adv. Mater. 24 (2012) 6034–6041, https://doi.org/10.1002/adma.201202744.

[12] Y. Son, S. Sim, H. Ma, M. Choi, Y. Son, N. Park, J. Cho, M. Park, Exploring critical factors affecting strain distribution 1D silicon-based nanostructures for Lithium-ion battery anodes, Adv. Mater. 30 (2018) 1705430, https://doi.org/10.1002/adma.201705430.

[13] Y. Li, K. Yan, H.W. Lee, Z. Lu, N. Liu, Y. Cui, Growth of conformal graphene cages on micrometre-sized silicon particles as stable battery anodes, Nat. Energy 1 (2016) 15029, https://doi.org/10.1038/nenergy.2015.29.

[14] N. Liu, H. Wu, M.T. McDowell, Y. Yao, C. Wang, Y. Cui, A yolk-shell design for stabilized and scalable Li-ion battery alloy anodes, Nano Lett. 12 (2012) 3315–3321, https://doi.org/10.1021/nl3014814.

[15] X. Li, M. Gu, S. Hu, R. Kennard, P. Yan, X. Chen, C. Wang, M.J. Sailor, J.G. Zhang, J. Liu, Mesoporous silicon sponge as an anti-pulverization structure for high-performance lithium-ion battery anodes, Nat. Commun. 5 (2014) 4105, https://doi.org/10.1038/ncomms5105.

[16] U. Kasavajjula, C. Wang, A.J. Appleby, Nano-and bulk-silicon-based insertion anodes for lithium-ion secondary cells, J. Power Sources 163 (2007) 1003–1039, https://doi.org/10.1016/j.jpowsour.2006.09.084.

[17] C.K. Chan, H. Peng, G. Liu, K. Mcllwrath, X.F. Zhang, R.A. Huggins, Y. Cui, High-performance lithium battery anodes using silicon nanowires, Nat. Nanotechnol. 3 (2008) 31–35, https://doi.org/10.1038/nnano.2007.411.

[18] H. Wu, G. Yu, L. Pan, N. Liu, M.T. McDowell, Z. Bao, Y. Cui, Stable Li-ion battery anodes by in-situ polymerization of conducting hydrogel to conformally coat silicon nanoparticles, Nat. Commun. 4 (2013) 1943, https://doi.org/10.1038/ncomms2941.

[19] D. Kim, S. Hyun, S.M. Han, Freestanding silicon microparticle and self-healing polymer composite design for effective lithiation stress relaxation, J. Mater. Chem. A 6 (2018) 11353–11361, https://doi.org/10.1039/C7TA11269F.

[20] M. Kim, S.P. Harvey, Z. Huey, S.D. Han, C.S. Jiang, S.B. Son, Z. Yang, I. Bloom, A new mechanism of stabilizing SEI of Si anode driven by crosstalk behavior and its potential for developing high performance Si-based batteries, Energy Storage Mater. 55 (2023) 436–444, https://doi.org/10.1016/j.ensm.2022.12.004.

[21] J. Kim, O.B. Chae, B.L. Lucht, Structure and stability of the solid electrolyte interphase on silicon anodes of lithium-ion batteries, J. Electrochem. Soc. 168 (2021) 030521, https://doi.org/10.1149/1945-7111/abe984.

[22] T. Yoon, C.C. Nguyen, D.M. Seo, B.L. Lucht, Capacity fading mechanisms of silicon nanoparticle negative electrodes for lithium ion batteries, J. Electrochem. Soc. 162 (12) (2015) A2325–A2330, https://doi.org/10.1149/2.0731512jes.

[23] W. Liu, H. Xu, H. Qin, Y. Lv, F. Wang, G. Zhu, F. Lin, F. Wang, C. Ni, The effect of carbon coating on graphite@nano-Si composite as anode materials for Li-ion batteries, J. Solid State Electrochem. 23 (2019) 3363–3372, https://doi.org/10.1007/s10008-019-04413-3.

[24] B. Liu, P. Huang, Z. Xie, Q. Huang, Large-scale production of a silicon nanowire/graphite composites anode via the CVD method for high-performance lithium-ion batteries, Energy Fuel 35 (2021) 2758–2765, https://doi.org/10.1021/acs.energyfuels.0c03725.

[25] W. Liu, H. Xu, H. Qin, Y. Lv, G. Zhu, X. Lei, F. Lin, Z. Zhang, L. Wang, Rapid coating of asphalt to prepare carbon-encapsulated composites of nano-silicon and graphite for lithium battery anodes, J. Mater. Sci. 55 (2020) 4382–4394, https://doi.org/10.1007/s10853-019-04313-x.

[26] X. Han, H. Chen, J. Liu, H. Liu, P. Wang, K. Huang, C. Li, S. Chen, Y. Yang, A peanut shell inspired scalable synthesis of three-dimensional carbon coated porous silicon particles as an anode for Lithium-ion batteries, Electrochim. Acta 156 (2015) 11–19, https://doi.org/10.1016/j.electacta.2015.01.051.

[27] X. Han, H. Chen, X. Li, J. Wang, C. Li, S. Chen, Y. Yang, Interfacial nitrogen stabilizes carbon-coated mesoporous silicon particle anodes 4 (2016) 434–442, https://doi.org/10.1039/C5TA08297H.

[28] H. Jia, X. Li, J. Song, X. Zhang, L. Luo, Y. He, B. Li, Y. Cai, S. Hu, X. Xiao, C. Wang, K.M. Rosso, R. Yi, R. Patel, J.G. Zhang, Hierarchical porous silicon structures with extraordinary mechanical strength as high-performance lithium-ion battery anodes, Nat. Commun. 11 (2020) 1474, https://doi.org/10.1038/s41467-020-15217-9.

[29] Q. Xia, K. Yan, K. Jin, Y. Wu, Y. Fu, D. Chen, H. Chen, H. Yue, Interface design of tea stem-derived micropore carbon enables high-performance Na-Se batteries, Chin. Chem. Lett. (2024) 110406, https://doi.org/10.1016/j.cclet.2024.110406.

[30] D. Shao, D. Tang, Y. Mai, L. Zhang, Nanostructured silicon/porous carbon spherical composite as a high capacity anode for Li-ion batteries, J. Mater. Chem. A 1 (2013) 15068–15075, https://doi.org/10.1039/c3ta13616g.

[31] H. Shi, W. Zhang, D. Wang, J. Wang, C. Wang, Z. Xiong, F.R. Chen, H. Dong, B. Xu, X. Yan, Facile preparation of silicon/carbon composite with porous architecture for

advanced lithium-ion battery anode, J. Electroanal. Chem. 937 (2023) 117427, https://doi.org/10.1016/j.jelechem.2023.117427.
[32] H. Chen, S. He, X. Hou, S. Wang, F. Chen, H. Qin, Y. Xia, G. Zhou, Nano-Si/C microsphere with hollow double spherical interlayer and submicron porous structure to enhance performance for lithium-ion battery anode, Electrochim. Acta 312 (2019) 242–250, https://doi.org/10.1016/j.electacta.2019.04.170C.
[33] C.-H. Cho, W.U. Jeong, C.-H. Lim, J.-K. Yoon, C.Y. Bon, K.-S. Yang, M.-S. Park, Facile synthesis of nano-si/graphite-carbon anode through microwave-induced carbothermal shock for lithium-ion batteries, Carbon 229 (2024) 119542, https://doi.org/10.1016/j.carbon.2024.119542.
[34] K.S. Yang, Y.J. Yoon, M.S. Lee, W.J. Lee, J.H. Kim, Further carbonization of anisotropic and isotropic pitch-based carbons by microwave irradiation, Carbon 40 (2002) 897–903, https://doi.org/10.1016/S0008-6223(01)00210-X.
[35] D.W. Kim, K.K. Im, H.J. Kim, D.H. Lee, Y.A. Kim, J. Choi, K.S. Yang, Effects of electromagnetic irradiation on low-molecular-weight fraction of fluidized catalytic cracking decant oil for synthesis of pitch precursor, J. Ind. Eng. Chem. 82 (2020) 205–210, https://doi.org/10.1016/j.jiec.2019.10.014.
[36] T. Kim, J. Lee, K.H. Lee, Microwave heating of carbon-based solid materials, Carbon Lett. 15 (2014) 15–24, https://doi.org/10.5714/CL.2014.15.1.015.
[37] M. Hotta, M. Hayashi, M.T. Lanagan, D.K. Argawal, K. Nagata, Complex permittivity of graphite, carbon black and coal powders in the ranges of X-band frequencies (8.2 to 12.4 GHz) and between 1 and 10 GHz, ISIJ Int. 51 (2011) 1766–1772, https://doi.org/10.2355/isijinternational.51.1766.
[38] Y. Bao, Y.S. Tay, T.-T. Lim, R. Wang, R.D. Webster, X. Hu, Polyacrylonitrile (PAN)-induced carbon membrane with in-situ encapsulated cobalt crystal for hybrid peroxymonosulfate oxidation-filtration process: preparation, characterization and performance evaluation, Chem. Eng. J. 373 (2019) 425–436, https://doi.org/10.1016/j.cej.2019.05.058.
[39] W. Zhang, X. Wei, T. Wu, F. Wei, L. Ma, Y. Lv, W. Zhou, H. Liu, Carbothermal shock enabled functional nanomaterials for energy-related applications, Nano Energy 118 (2023) 108994, https://doi.org/10.1016/j.nanoen.2023.108994.
[40] Y. Zhou, A. Yin, L. Cao, Y. Wan, Guo, efficient 3D conducting networks built by graphene sheets and carbon nanoparticles for high-performance silicon anode, ACS Appl. Mater. Interfaces 4 (5) (2012) 2824–2828, https://doi.org/10.1021/am3005576.
[41] D.-L. Fang, Y.-C. Zhao, S.-S. Wang, T.-S. Hu, C.-H. Zheng, Highly efficient synthesis of nano-Si anode material for Li-ion batteries by a ball-milling assisted low-temperature aluminothermic reduction, Electrochim. Acta 330 (2020) 135346, https://doi.org/10.1016/j.electacta.2019.135346.
[42] L. Wu, F. Pei, R. Mao, F. Wu, Y. Wu, J. Qian, Y. Cao, X. Ai, H. Yang, SiC–Sb–C nanocomposites as high-capacity and cycling-stable anode for sodium-ion batteries, Electrochim. Acta 87 (2013) 41–45, https://doi.org/10.1016/j.electacta.2012.08.103.
[43] G. Velpula, R. Phillipson, J.X. Lian, D. Cornil, P. Walke, K. Verguts, S. Breams, H. Uji-I, S.D. Gendt, D. Beljonne, R. Lazzaroni, K.S. Mali, S.D. Feyter, Graphene meets ionic liquids: Fermi level engineering via electrostatic forces, ACS Nano 13 (3) (2019) 3512–3521, https://doi.org/10.1021/acsnano.8b09768.
[44] S.Y. Kim, J. Lee, B.H. Kim, Y.-J. Kim, K.S. Yang, M.-S. Park, Facile synthesis of carbon-coated silicon/graphite spherical composites for high-performance lithium-ion batteries, ACS Appl. Mater. Interfaces 8 (19) (2016) 12109–12117, https://doi.org/10.1021/acsami.5b11628.
[45] R. Patil, M. Phadatare, N. Blomquist, J. Örtegren, M. Hummelgård, J. Meshram, D. Dubal, H. Olin, Highly stable cycling of silicon-nanographite aerogel-based anode for lithium-ion batteries, ACS Omega 6 (10) (2021) 6600–6606, https://doi.org/10.1021/acsomega.0c05214.
[46] S.P.V. Nadimpalli, V.A. Sethuraman, S. Dalavi, B. Lucht, M.J. Chon, V.B. Shenoy, P. R. Guduru, Quantifying capacity loss due to solid-electrolyte-interphase layer formation on silicon negative electrodes in lithium-ion batteries, J. Power Sources 215 (2012) 145–151, https://doi.org/10.1016/j.jpowsour.2012.05.004.
[47] W. Choi, H.-C. Shin, J.M. Kim, J.-Y. Choi, W.-S. Yoon, Modeling and applications of electrochemical impedance spectroscopy (EIS) for Lithium-ion batteries, J. Electrochem. Sci. Technol. 11 (1) (2020) 1–13, https://doi.org/10.33961/jecst.2019.00528.